Kobe University Repository : Kernel

PDF issue: 2026-11-17

A hybrid experimental-numerical study on the mechanism of three-dimensional dynamic fracture

Nishioka, Toshihisa

Stan, F.

(Citation)
Computer Modeling in Engineering & Sciences : CMES,4(1):119-139

(Issue Date)
2003

(Resource Type)
journal article

(Version)
Accepted Manuscript

(URL)
https://hdl.handle.net/20.500.14094/90000037

R450

A Hybrid Experimental-Numerical Study on the Mechanism of Three-Dimensional Dynamic Fracture

T. Nishioka[1] *and F. Stan*[1]

Contents

1 Introduction 1
2 Experimental Results 2
3 Moving Finite Element Method 4
3.1 Automatic element-control method 4
3.2 Time integration method 6
4 Generation Phase Simulations of Dynamic Fracture Experiments 7
5 Three-Dimensional Dynamic Fracture Parameters 8
5.1 Dynamic J integral 8
5.2 Dynamic stress intensity factor 9
5.3 Distribution of dynamic J integral 9
5.4 Distribution of dynamic stress intensity factor 11
6 Three-Dimensional Stress Fields for Naturally Propagating Cracks 14
6.1 Stress variation through thickness 14
6.2 Variation of the stress-triaxiality parameter 14
7 Discussion and Conclusions 16
Acknowledgements: 17
References: 17

A Hybrid Experimental-Numerical Study on the Mechanism of Three-Dimensional Dynamic Fracture

T. Nishioka[1] and F. Stan[1]

Abstract In this paper we investigate the essentially unexplored area of three-dimensional dynamic fracture mechanics. The general objective sought by this investigation is the understanding of three-dimensional dynamic crack propagation and arrest, and, specifically, the effect that the specimen thickness has on the dynamic fracture mechanism. In particular, in the context of the present paper, it is intended to provide a summary of the achievements on the issue of three-dimensional dynamic fracture parameters. Furthermore, the behavior of the three-dimensional field near the crack front is investigated. The issue that will be addressed is the extent of regions over which plane stress and plane strain analyses provide a good approximation to the actual three-dimensional fields. The results obtained in this paper offer some important new insights into the effect of the specimen thickness on dynamic fracture.

keyword: Dynamic fracture, three-dimensional fracture, fracture mechanism, moving finite element method, fracture toughness, thickness effect, dynamic J integral, dynamic stress intensity factor, stress-triaxiality parameter.

1 Introduction

While much of the current research and development effort is devoted to expanding fracture mechanics into two-dimensional dynamically loaded specimens or structures, there has been a little progress made in understanding the various aspects of three-dimensional dynamic fracture. In three-dimensional dynamic fracture phenomena, there have been many unsolved problems. For example, (i) What is the shape of the dynamically propagating crack front after fracture? (ii) What is the distribution of the fracture parameters along the propagating crack front? (iii) Do plane strain conditions prevail at the crack front inside of the plate? (iv) Do plane stress conditions prevail at the free surface of the plate? (v) What is the stress singularity at the corner where the actual crack front meets the free surface of the plate? (vi) What is the effect that the specimen thickness has on the mechanism of the fracture?

Some of the aforementioned problems have been partly solved by our previous experimental and numerical studies on three-dimensional dynamic fracture phenomena. For example, Nishioka, Yoshimura, Nishi and Sakakura (1995) firstly succeeded in precise continuous measurements of the shapes of dynamically propagating curved crack fronts in Double Cantilever Beam (DCB) specimens with various thicknesses. The transparency of PMMA (Polymethyl-methacrylate) and a high-speed photography system made it possible to visualize the dynamically propagating crack fronts inside of three-dimensional solids.

They found the following major points from the experimental results: (1) The curvatures of the dynamically propagating crack fronts in the DCB specimens increase with increasing plate thickness, but they saturate to a maximum curvature near the plate thickness of 15 mm. The dynamically propagating crack fronts in specimens thinner than 5 mm are almost straight. (2) In the thicker specimens, the curvatures decrease with increasing crack velocity. (3) The singularities at the corner points of the arrested crack fronts decrease with increasing plate thickness and approach the crack-tip singularity at the inside of an elastic solid.

Furthermore, in the numerical study on three-dimensional dynamic fracture [Nishioka, Ichikawa and Maeda (1995)], first, an equivalent domain integral expression of the dynamic J integral [Nishioka and Atluri (1983a)] was derived for three-dimensional dynamic fracture mechanics. Next, in order to simulate three-dimensional dynamic crack propagation, a three-dimensional moving finite element method was developed. The moving finite element procedure together with the dynamic J integral evaluation procedure made it possible to evaluate the distribution of the dynamic energy release rate along the propagating crack front at each time step.

In a more recent numerical study, Nishioka, Stan and Fujimoto (2002) firstly succeeded to evaluate the fracture parameters such as the dynamic stress intensity factor or the dynamic J integral for naturally and dynamically propagating crack fronts. The experimentally observed three-dimensional dynamic fracture phenomenon [Nishioka, Yoshimura, Nishi and Sakakura (1995)] in the DCB specimen of 20mm thickness was regenerated and simulated in the computational

[1]Simulation Engineering Laboratory, Department of Ocean Mechanical Engineering, Kobe University of Mercantile Marine, Higashinada-Ku, Kobe, 658-0022, Japan

model based on the moving finite element method together with the automatic element-control method. It was found that the dynamic J integral and the dynamic stress intensity factor are almost constant along the naturally and dynamically propagating and arresting curved crack fronts, even at the corner points where the crack front intersects the free surfaces of the plate.

In this paper, based on the newly developed simulation technologies [Nishioka, Stan and Fujimoto (2002)], the generation-phase simulations are carried out using the experimentally recorded histories of three-dimensional dynamic fracture events in the DCB specimens with different thickness. Regenerating the dynamic fracture phenomena in the computational model, the distributions of the fracture parameters along the actual dynamic fracture fronts are elucidated. The effects of the specimen thickness on three-dimensional dynamic fracture behavior are also firstly elucidated.

2 Experimental Results

Usually, an experiment plays a central role in establishing the understanding of dynamic fracture phenomena. However, an experimental measurement is almost impossible to obtain the detailed information on the fracture parameters along the dynamically propagating crack front embedded in the inside of the solid. Thus, in case of three-dimensional fracture, one of the most important pieces of information is the shape of dynamically propagating crack front.

To the author's knowledge, precise continuous measurements of dynamically propagating crack fronts had not been made until the experimental study done by Nishioka, Yoshimura, Nishi and Sakakura (1995). In this experimental study, using a high-speed camera, high-speed photographs of dynamically propagating crack fronts in the DCB specimens of PMMA were systematically recorded. The in-plane geometry of the DCB specimen is illustrated in Fig. 1.

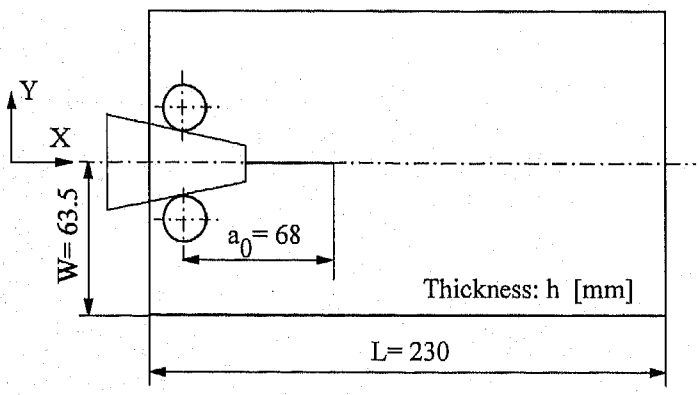


Figure 1: Specimen geometry

The material properties as well as the dilatational, shear and Rayleigh wave velocities in this material are presented in Table 1. PMMA is transparent and has the refractive index of 1.49. Since the refractive index is greater than $\sqrt{2}$, PMMA has the mirror-like fracture surface, which made it possible to visualize instantaneous shapes of dynamically propagating crack fronts.

A displacement-controlled load was applied to the specimen through a wedge between the pins inserted into the loading pin holes. The load and the load-point displacement were recorded during the experiment.

Selected high-speed photographs for the thinner and thicker specimens are presented in Fig. 2. The numbers in the photographs indicate the time in microsecond (μsec) after the initiation of the brittle fracture.

Table 1: Mechanical properties of PMMA

Poisson's ratio	ν	0.39
Young's modulus	E [GPa]	2.94
Mass density	ρ [κg/m^3]	1190
Refractive index	n	1.49
Dilatational wave velocity	C_d [m/s]	2220
Shear wave velocity	Cs [m/s]	943
Rayleigh wave velocity	C_R [m/s]	886

Table 2: The records of high-speed photographs

Specimen No.	3D-1	3D-2	3D-6	3D-8	3D-10
First photograph t_0 [μsec]	50.1	72.8	63.29	49.2	55.6
Crack arrest time [μsec]	230	302	243	368	246

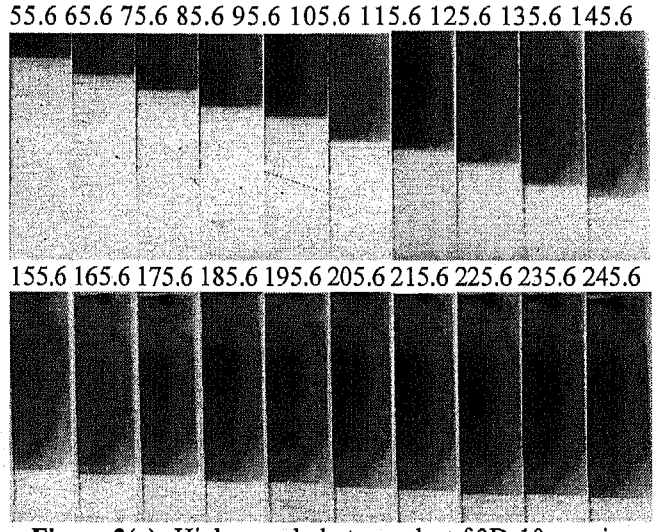


Figure 2(a): High-speed photographs of 3D-10 specimen

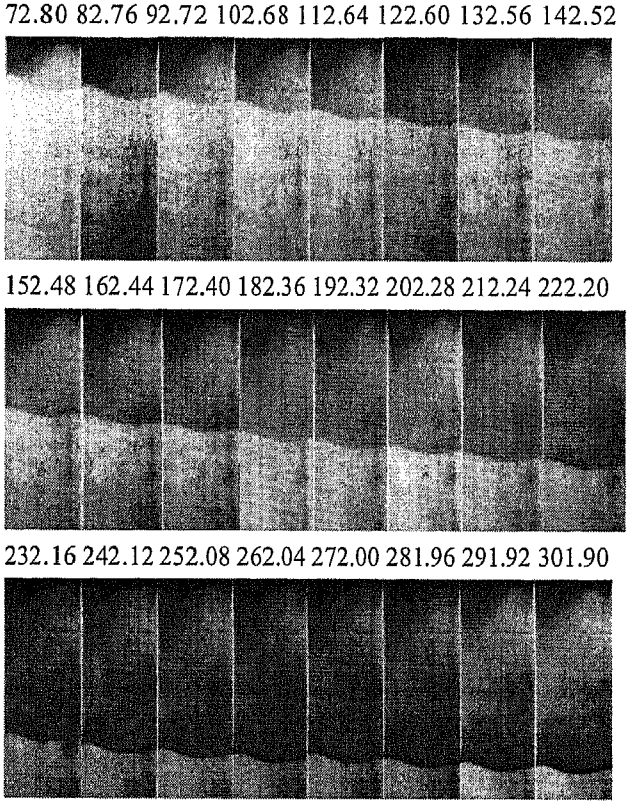


Figure 2(b): High-speed photographs of 3D-2 specimen

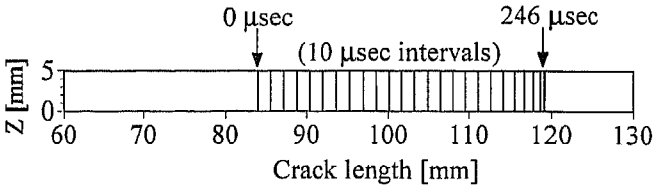
Because of the delay of the trigger system the first photograph was recorded at time t_0 (see Table 2) after the onset of brittle fracture. The experimental conditions are listed in Table 3.

The variations of the crack-front shapes during dynamic propagation and arrest are shown in Fig. 3. It should be noted that before time t_0 (see Table 2), the crack is assumed to propagate as natural extension of the experimentally measured data.

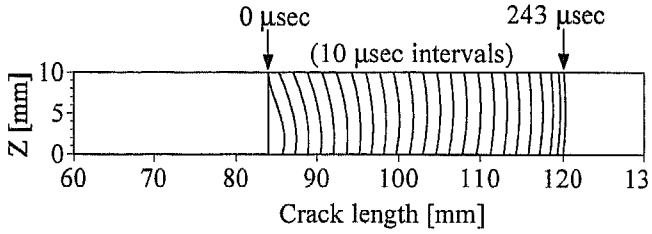
It can be seen that in the thinner specimen (see Fig. 3(a)) the crack propagated with an almost straight crack front, while in the thicker specimens (see Figs. 3(b), (c), (d) and (e)), the crack started to propagate from the off-centered initiation point along the initial notch front. Also, one can see that in the thicker specimen the crack front at the center of the specimen went in advance of those at the plate surfaces.

Table 3: Experimental conditions

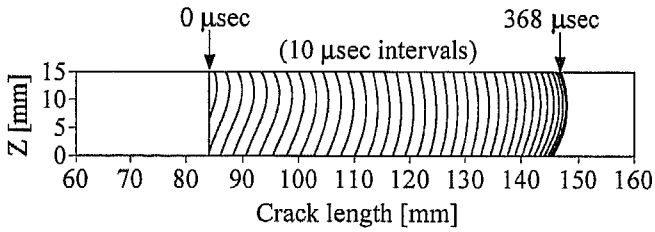
Specimen No.	Wedge Load at Fracture P_w [kN]	Thickness h [mm]	Ambient Temperature T [°C]	Initial Notch Radius [mm]
3D-1	1.31	20	17	0.45
3D-2	1.63	20	22	0.45
3D-6	1.231	15	28	0.35
3D-8	0.572	10	13.8	0.35
3D-10	0.248	5	15.6	0.25



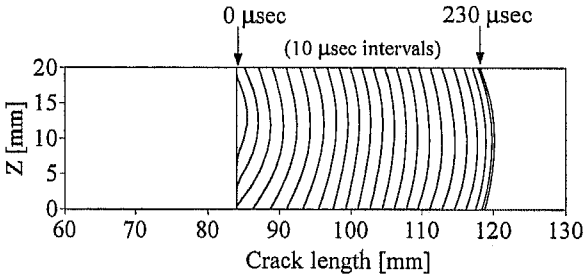
(a) 3D-10 specimen



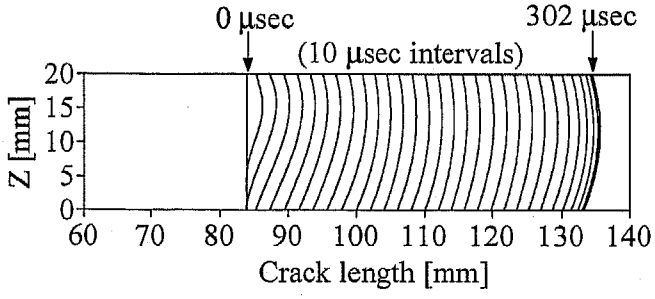
(b) 3D-8 specimen



(c) 3D-6 specimen



(d) 3D-1 specimen



(e) 3D-2 specimen

Figure 3: Variation of crack-front shapes during dynamic crack propagation and arrest

In the early stage of propagation in the thicker specimens, the crack fronts were greatly unsymmetrical, but, gradually, a stage of steady crack growth was reached, and crack fronts became almost symmetrical. The curvatures of the dynamically propagating crack fronts increase with increasing thickness of the plate, and the distance of dynamic crack propagation up to the crack arrest increases considerably with increasing input energy per unit thickness into the specimen by applied load priori to the onset of dynamic fracture [Nishioka, Yoshimura, Nishi and Sakakura (1995)].

3 Moving Finite Element Method

For fracture simulations, numerical analysis methods such as the finite element methods can be classified into two types [Nishioka and Atluri (1986); Nishioka (1994, 1997)]: (i) fixed element methods and (ii) moving element methods.

In general, the fixed finite element procedure has the following severe disadvantages:

(1) The boundary conditions in front of and behind the propagating crack tip or front cannot be satisfied exactly.
(2) The violation of the boundary conditions produces spurious numerical error waves in the model.
(3) The fixed mesh pattern may not fit with the actual fracture front and fracture paths.

Especially, these situations become worse when the fixed element methods are used for three-dimensional dynamic fracture problems with curved crack fronts.

Nishioka et al. [Nishioka and Atluri (1980); Nishioka and Takemoto (1989); Nishioka Tokudome and Kinoshita (2001); Nishioka, Furutuka, Tchouikov, Fujimoto (2002)] developed many types of moving finite element procedures. In order to overcome the difficulties in three-dimensional crack propagation, Nishioka, Ichikawa and Maeda (1995) developed a 20-noded moving isoparametric element method for straight crack fronts. Furthermore, Nishioka, Stan and Fujimoto (2002) have extended the moving 20-noded isoparametric element method for dynamically propagating curved crack fronts.

The 20-noded isoparametric elements used in the mesh are divided into three types: Type A: moving elements near the crack front (see Figs. 4 and 5), Type B: distorting elements, Type C: non-distorting elements, respectively. Type A elements near the crack front translate in each time step for which crack growth occurs. Type B elements (see Fig. 5) surrounding the moving elements are continuously distorted.

As shown in Fig. 5, the mesh pattern for the elements near the crack tip translates in each time step for which the crack growth occurs. Thus, the crack tip always remains at the center of the moving elements throughout the analysis. The translation of the crack tip for each time step can take any value and is not related to the assumed discretization. In order to simulate a large amount of crack propagation, the mesh pattern around the moving elements is periodically shifted and readjusted as shown in Fig. 5.

3.1 Automatic element-control method

In order to simulate two-dimensional dynamic crack curving, Nishioka, Murakami and Takemoto (1990) developed the moving isoparametric element method based on a mapping technique. In the previous paper [Nishioka, Stan and Fujimoto (2002)] the mapping technique was extended to three-dimensional crack propagation problems with curved crack fronts. Based on the mapping technique, an automatic element-control method was developed (see Figs. 4 and 5).

The mesh pattern in the real body is created by the mapping from the element-controlling body through a mapping function (see Fig. 4). The mapping function consists of several Lagrangian elements. The shape functions of the Lagrangian element are given by:

$$N_{kji} = L_k^m(\xi) \cdot L_j^n(\lambda) \cdot L_i^p(\eta), \tag{1}$$

where $L_k^m(\xi)$, $L_j^n(\lambda)$ and $L_i^p(\eta)$ are the Lagrange's polynomials, and are defined by

$$L_k^m(\xi)=\frac{(\xi-\xi_1)\cdots(\xi-\xi_{k-1})(\xi-\xi_{k+1})\cdots(\xi-\xi_m)}{(\xi_k-\xi_1)\cdots(\xi_k-\xi_{k-1})(\xi_k-\xi_{k+1})\cdots(\xi_k-\xi_m)}; \tag{2}$$

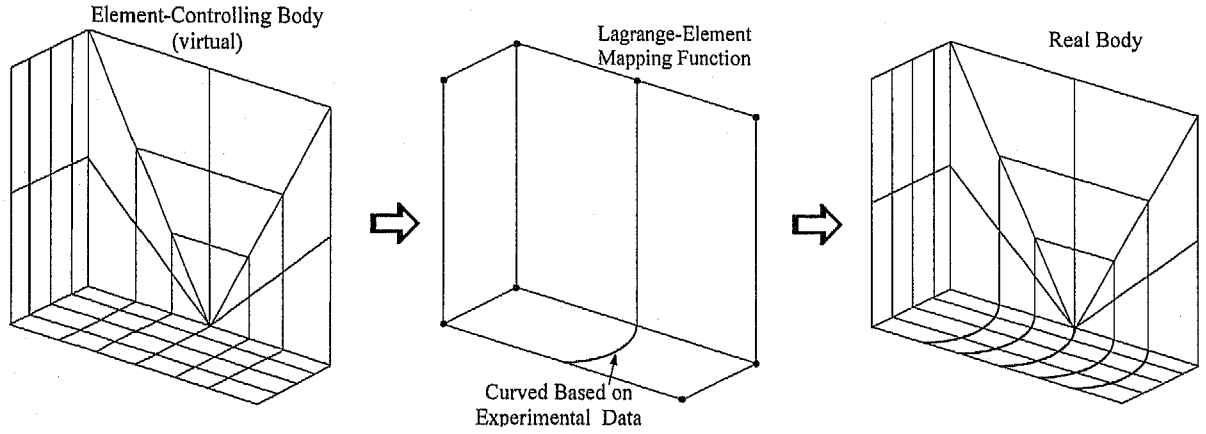


Figure 4: Mapping between an element-controlling body and a real body (Type A elements)

$$L_j^n(\lambda)=\frac{(\lambda-\lambda_1)\cdots(\lambda-\lambda_{j-1})(\lambda-\lambda_{j+1})\cdots(\lambda-\lambda_n)}{(\lambda_j-\lambda_1)\cdots(\lambda_j-\lambda_{j-1})(\lambda_j-\lambda_{j+1})\cdots(\lambda_j-\lambda_n)}, \quad (3)$$

$$L_i^p(\eta)=\frac{(\eta-\eta_1)\cdots(\eta-\eta_{i-1})(\eta-\eta_{i+1})\cdots(\eta-\eta_p)}{(\eta_i-\eta_1)\cdots(\eta_i-\eta_{i-1})(\eta_i-\eta_{+1})\cdots(\eta_i-\lambda_p)}, \quad (4)$$

in which ξ_k denotes the natural coordinate value of the k-th node in the ξ direction.

Any point $P_v(x_v, y_v, z_v)$ on the virtual element-controlling body is mapped onto a point $P_r(x_r, y_r, z_r)$ on the real body according to the following relation:

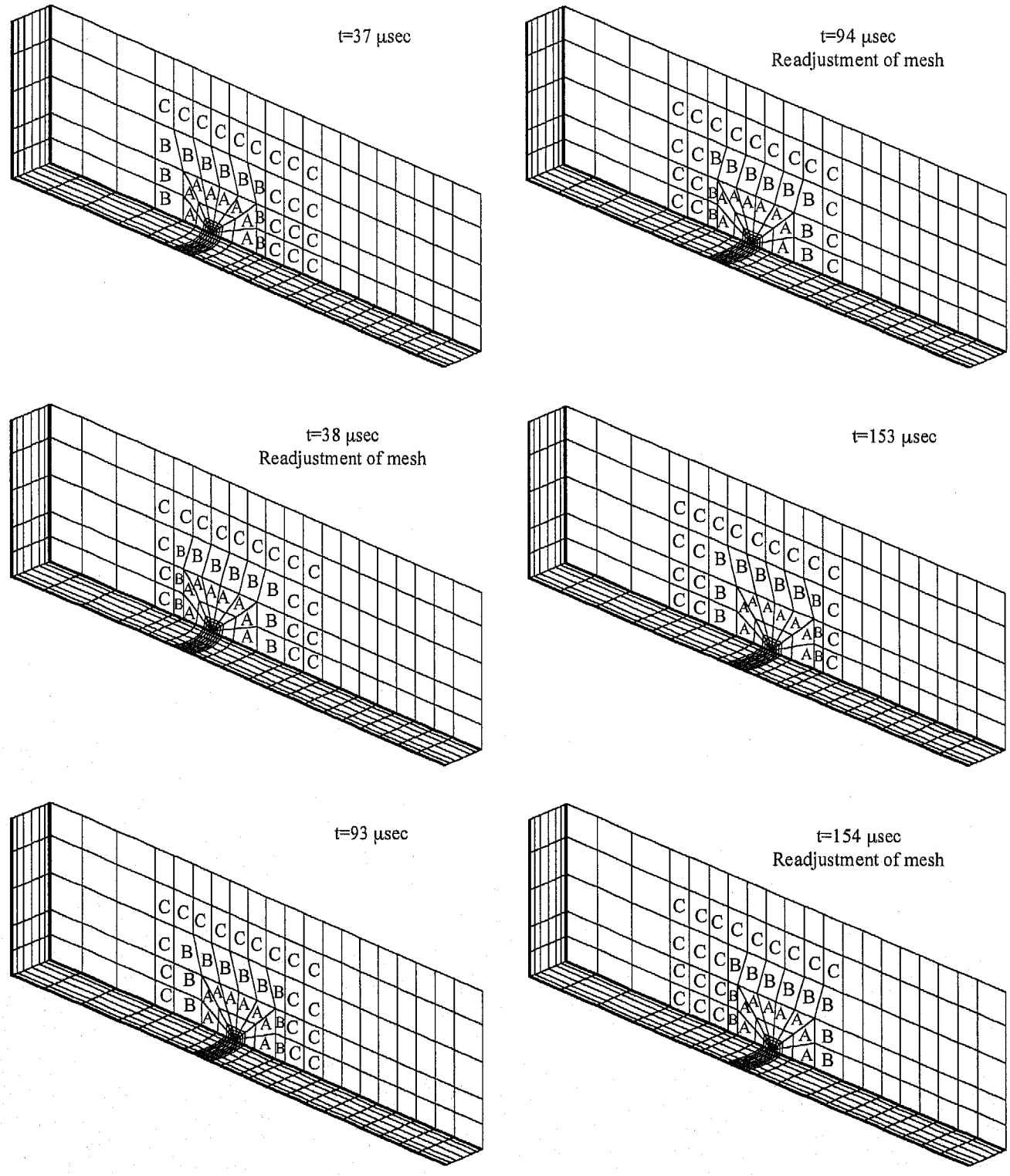


Figure 5: Mesh movement and readjustment procedure

$$\begin{Bmatrix} x_r \\ y_r \\ z_r \end{Bmatrix} = \sum_{k=1}^{m} \sum_{j=1}^{n} \sum_{i=1}^{p} N_{kji}(\xi_v, \lambda_v, \eta_v) \begin{Bmatrix} x_{r\,kji} \\ y_{r\,kji} \\ z_{r\,kji} \end{Bmatrix}, \quad (5)$$

where ξ_v, λ_v, η_v are the natural coordinate values of the point $P_v(x_v, y_v, z_v)$ in the Lagrangian element, and $(x_{r\,kji}, y_{r\,kji}, z_{r\,kji})$ are the nodal coordinates of the Lagrangian element. The Lagrangian-element mapping function can be obtained using only the coordinates of curved crack front and external boundaries of the entire moving zone. The procedure of the mesh movement and readjustment are automatically controlled in the element-controlling body.

3.2 *Time integration method*

In this study, the Newmark method is used for the time integration of the finite element equation of motion. At a generic time step n, the final form of the finite element equation of motion to be solved is expressed as [Nishioka, Stan and Fujimoto (2002)]:

$$\left(a_0[M]^{(n)}+[K]^{(n)}\right)\{Q\}_n^{(n)} = \{F\}_n^{(n)}+[M]^{(n)}\left(a_0\{Q\}_{n-1}^{(n)}+a_2\{\dot{Q}\}_{n-1}^{(n)}+a_3\{\ddot{Q}\}_{n-1}^{(n)}\right), \quad (6)$$

where $\{Q\}$, $\{\dot{Q}\}$, $\{\ddot{Q}\}$ are the global vectors of nodal displacements, nodal velocities and nodal accelerations, respectively; *[M], [K]* and *[F]* are the consistent mass matrix, the stiffness matrix and the load vector, respectively. The subscripts n and $n-1$ denote the quantities at the present step n and at the previous time step $n-1$, respectively, while the superscript (n) denotes the quantities in the mesh pattern of the present time step n.

After solving Eq. (6) for nodal displacements at the present time step, the nodal velocities and accelerations can be evaluated by the following equations:

$$\{\ddot{Q}\}_n^{(n)} = a_0\left(\{Q\}_n^{(n)} - \{Q\}_{n-1}^{(n)}\right) - a_2\{\dot{Q}\}_{n-1}^{(n)} - a_3\{\ddot{Q}\}_{n-1}^{(n)}, \quad (7)$$

$$\{\dot{Q}\}_n^{(n)} = \{\dot{Q}\}_{n-1}^{(n)} + a_6\{\ddot{Q}\}_{n-1}^{(n)} + a_7\{\ddot{Q}\}_n^{(n)}. \quad (8)$$

The coefficients a_0~a_6 are the parameters in the Newmark method, and are given by

$$a_0 = \frac{1}{\beta(\Delta t_n)^2}, \quad a_1 = \frac{\delta}{\beta \Delta t_n}, \quad a_2 = \frac{1}{\beta \Delta t_n}, \quad a_3 = \frac{1}{2\beta} - 1, \quad a_4 = \frac{\delta}{2\beta} - 1,$$
$$a_5 = \frac{\Delta t_n}{2}\left(\frac{\delta}{\beta} - 2\right), \quad a_6 = \Delta t_n(1-\delta), \quad a_7 = \delta \Delta t_n. \quad (9)$$

To use the Newmark time integration scheme for the moving finite element method, the previous solutions fields for the current mesh pattern are needed, i.e., $\{Q\}_{n-1}^{(n)}$, $\{\dot{Q}\}_{n-1}^{(n)}$, $\{\ddot{Q}\}_{n-1}^{(n)}$. This means that the mapping of the solution fields in the previous mesh onto those in the present mesh is needed.

For a newly created node p due to the mesh movement and readjustment, these conversions can be done as follows:

$$(u_p)_{n-1}^{(n)} = \sum_{i=1}^{20} N_i^{(n-1)}(\xi_p, \eta_p, \zeta_p)(u_i)_{n-1}^{(n-1)}; \text{(p=1, 2,···, N)} \quad (10)$$

$$(v_p)_{n-1}^{(n)} = \sum_{i=1}^{20} N_i^{(n-1)}(\xi_p, \eta_p, \zeta_p)(v_i)_{n-1}^{(n-1)}; \text{(p=1, 2,···, N)} \quad (11)$$

$$(w_p)_{n-1}^{(n)} = \sum_{i=1}^{20} N_i^{(n-1)}(\xi_p, \eta_p, \zeta_p)(w_i)_{n-1}^{(n-1)}; \text{(p=1, 2,···, N)} \quad (12)$$

$$(\dot{u}_p)_{n-1}^{(n)} = \sum_{i=1}^{20} N_i^{(n-1)}(\xi_p, \eta_p, \zeta_p)(\dot{u}_i)_{n-1}^{(n-1)}; \text{(p=1, 2,···, N)} \quad (13)$$

$$(\dot{v}_p)_{n-1}^{(n)} = \sum_{i=1}^{20} N_i^{(n-1)}(\xi_p, \eta_p, \zeta_p)(\dot{v}_i)_{n-1}^{(n-1)}; \text{(p=1, 2,···, N)} \quad (14)$$

$$(\dot{w}_p)_{n-1}^{(n)} = \sum_{i=1}^{20} N_i^{(n-1)}(\xi_p, \eta_p, \zeta_p)(\dot{w}_i)_{n-1}^{(n-1)}; \text{(p=1, 2,···, N)} \quad (15)$$

$$(\ddot{u}_p)_{n-1}^{(n)} = \sum_{i=1}^{20} N_i^{(n-1)}(\xi_p, \eta_p, \zeta_p)(\ddot{u}_i)_{n-1}^{(n-1)}; \text{(p=1, 2,···, N)} \quad (16)$$

$$(\dot{v}_p)_{n-1}^{(n)} = \sum_{i=1}^{20} N_i^{(n-1)}(\xi_p, \eta_p, \zeta_p)(\dot{v}_i)_{n-1}^{(n-1)}; \text{(p=1, 2,···, N)} \quad (17)$$

$$(\ddot{w}_p)_{n-1}^{(n)} = \sum_{i=1}^{20} N_i^{(n-1)}(\xi_p, \eta_p, \zeta_p)(\ddot{w}_i)_{n-1}^{(n-1)}; \text{(p=1, 2,···, N)}, \quad (18)$$

where u, v and w are the displacement components in the global coordinate system. N is the number of nodes in the moving and distorting elements or in the element to be readjusted (see Fig. 5).

To calculate the conversion equations (10) to (18), two

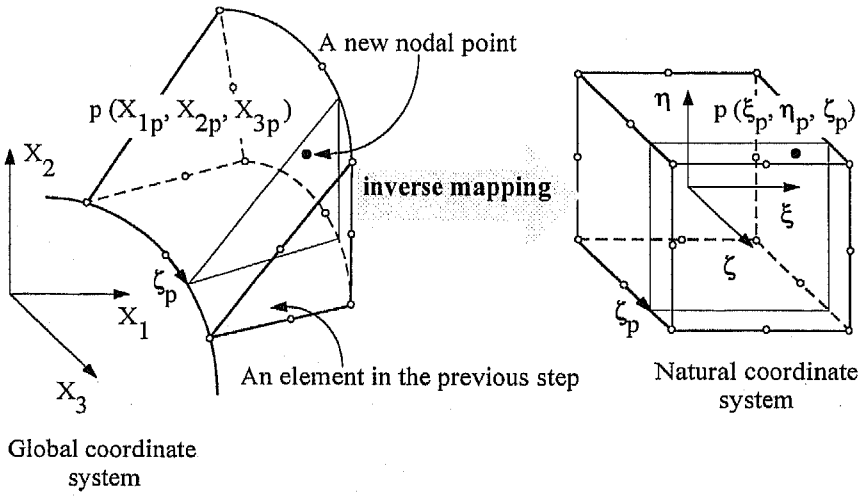


Figure 6: Inverse mapping for a 20–noded isoparametric element

automatic schemes were developed [Nishioka, Stan and Fujimoto (2002)]: One scheme automatically finds an old element that includes a newly created node (see the point p in Fig. 6) after moving or readjusting the element around the propagating crack front.

Another scheme automatically finds the natural coordinates (ξ_p, η_p, ζ_p) in the old element (see Fig. 6), corresponding to the global coordinates (X_{1p}, X_{2p}, X_{3p}) of the newly created node p. In this scheme, first, ζ_p is determined by the following equation since the right and left surfaces of the element are parallel:

$$\zeta_p = \frac{(2X_{3p} - X_{3pr} - X_{3pl})}{(X_{3pr} - X_{3pl})}, \tag{19}$$

where X_{3pr} and X_{3pl} are the X_3 coordinate values of the right and left sides of the element. In previous studies, the inverse mapping formulas for two-dimensional 8-noded isoparametric elements were obtained by using a computerized symbolic manipulation [Nishioka and Takemoto (1989); Nishioka (1995)]. In the present scheme for the three-dimensional 20-noded isoparametric elements, the same explicit expressions for the inverse mapping formulas [Nishioka (1995)] for finding ξ_p and η_p are utilized.

An extremely important feature that distinguishes the moving element procedures from the fixed element procedures with various nodal release techniques often used in literature is that the displacement boundary conditions ahead of the propagating crack tip can be satisfied exactly in the moving element procedures.

As explained here, the moving finite element method has great advantageous features. A possible alternative to the moving finite element method may be the Messless Local Petrov-Galerkin (MLPG) Method [Atluri and Zhu (1998); Kim and Atluri (2000)]. Using the MLPG method, Ching and Batra (2001) successfully analysed the two-dimensional singular stress field near a crack tip.

For three-dimensional crack problems, Nishioka and Atluri (1983b) developed the finite element alternating method using the VNA solution [Vijayakumar and Atluri (1981); Nishioka and Atluri (1983b)] of an elliptical crack. The VNA-FEM alternating method was applied to various elliptical and part-elliptical crack problems [Nishioka and Atluri (1982, 1983b, 1983c); O'Donoghue, Nishioka and Atluri (1984)]. Recently Nikishkov, Park and Atluri (2001) replaced the VNA solution with the Symmetric Galerkin Boundary Element Method, and developed SGBEM-FEM alternating method for the analysis of three-dimensional non-planar cracks, and their growth.

4 Generation Phase Simulations of Dynamic Fracture Experiments

In the generation-phase simulation [Kanninen (1978), Nishioka (1997)] the experimentally observed fracture phenomenon is regenerated in the computer model using the

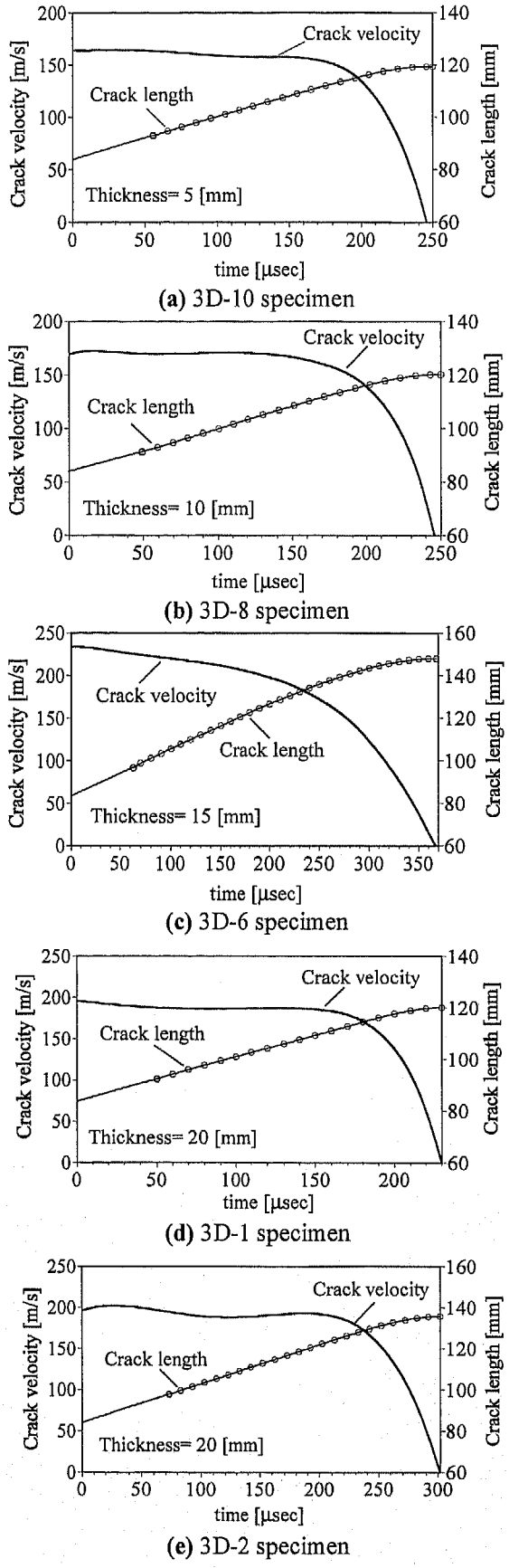


Figure 7: Crack propagation history

experimental conditions and experimentally measured fracture data such as crack propagation history and information on crack-front shapes. The generation-phase simulation can be considered as one of the techniques classified into the hybrid experimental-numerical method [Kobayashi (1983); Atluri and Nishioka (1984); Nishioka (2000)].

The crack propagation histories at the mid-thickness of the plate are summarized in Fig. 7. The circle points in the figure are the experiment data, while the solid lines are two-dimensional least square fitted curves (see Fig. 3). Figures 3 and 7 are used as the input data for the generation phase simulation. The crack propagates with an almost constant velocity in most stage and decreases monotonically as the crack approaches arrest.

In the finite element analysis, the double cantilever beam (DCB) specimens presented in Fig.1 were modeled with 20-noded isoparametric elements. Since the fracture paths were straight along the X-axis (see Fig. 1), only mode I crack propagation is considered here. Thus, due to the symmetry of the geometry and the loading condition, only the upper part of the specimen was modeled in the present analyses.

The finite element mesh pattern for the initial configuration is shown in Fig. 8. The far-field paths for the dynamic J integral are also shown in Fig. 8. The mesh consists of 1400 elements and 6841 nodes. Ten layers of 20-noded isoparametric moving element through the thickness were used. It should be noted that the layers become thinner as the free surfaces are approached in order to model the corner point. For the generation phase-simulations the time increment of Δt=1μsec is used.

The mesh pattern for the elements near the crack tip translates in each time step according to the experimentally recorded history of crack propagation and arrest (see Fig. 3). The mesh movement for the 20 mm thick specimen is demonstrated in Fig. 5.

The wedge load P_w at the onset of fracture (see Table 3) is converted to the pin loads in the Y direction by the following formula:

$$P_Y = \frac{P_W}{2\{\tan(\theta_W/2)+\mu_f\}}, \tag{20}$$

where θ_w is the angle of the wedge and μ_f is the friction coefficient between the surfaces of the wedge and loading pins. In the experiments [Nishioka, Yoshimura, Nishi and Sakakura (1995)], the wedge with θ_w =20° was used. Since the surfaces of the wedge and loading pins were polished and furthermore lubricant was put between the surfaces, it can be considered that the friction coefficient is negligible (μ_f =0).

In order to start the generation-phase simulation, first, a trial static analysis was carried out applying a prescribed displacement at the centerline of the loading pin (X=16mm, Y=20mm and Z=0~h) through the specimen thickness. Using the ratio of the actual fracture load P_Y to the total reaction force calculated in the trial static analysis, the whole solution field and the actual loading displacement at the onset of fracture are obtained by the proportionality in the elastostatic problem. This loading displacement was applied throughout the simulation, since in each experiment a very slow displacement-controlled load was applied by the wedge.

5 Three-Dimensional Dynamic Fracture Parameters

Before summarizing the results, it might be useful to review some of the developed concepts, which bear upon the numerical analysis.

5.1 Dynamic J integral

In the numerical analysis, the equivalent domain integral (EDI) expression [Nishioka, Ichikawa and Maeda (1995); Nishioka, Stan and Fujimoto (2002)] of the dynamic J integral [Nishioka and Atluri (1983a)] has been used to compute the dynamic J integral values at all nodes along the three-dimensional crack fronts.

The general expression of dynamic J integral in terms of equivalent domain integral (EDI) method can be written as:

$$J'_k = \frac{1}{f}\left\{\int_{V_\Gamma}[\sigma_{ij}u_{i,k}s_{,j}-(W+K)s_{,k}+(\rho\ddot{u}_i\,u_{i,k}-\rho\dot{u}_i\,\dot{u}_{i,k})s\,]dV + \int_{\Gamma_1+\Gamma_2}[(W+K)n_k - t_i\,u_{i,k}]s\,dS\right\} \tag{21}$$

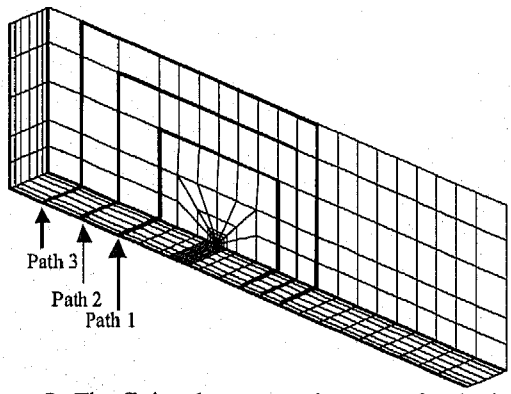


Figure 8: The finite element mesh pattern for the initial configuration

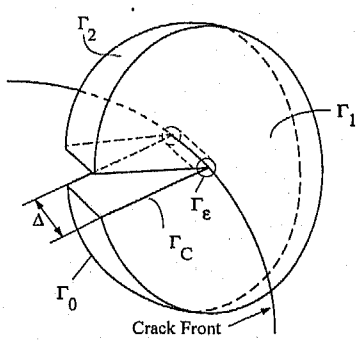


Figure 9: Integral paths

where W and K are the strain and kinetic energy densities, respectively; n_k are the outward normal-direction cosines; u_i, $\dot{u}_i$ and $\ddot{u}_i$ are displacement, velocity and acceleration of a material point, respectively; ρ is the mass density; s is a continuous function and f is the integral value of the s function along a crack-front segment (see Fig. 9) under consideration [Nikishkov and Atluri (1987); Nishioka, Ichikawa and Maeda (1995); Nishioka, Stan and Fujimoto (2002)]. The integral paths are defined according to Fig. 9.

The local components of the dynamic J integral (J'^0_l) are determined from the global-axis components of the dynamic J integral (J'_k) through the coordinate transformation [Nishioka and Atluri (1984)] (see Fig. 10):

$$J'^0_l = \alpha_{l\,k}\, J'_k, \tag{22}$$

where $\alpha_{l\,k}$ is the coordinates transformation tensor from the global coordinates X_k $(k=1, 2, 3)$ to the crack front coordinates x^0_l $(l=1, 2, 3)$.

The tangential component of the dynamic J integral J'^0_1 has the physical significance of the dynamic energy release rate G.

The EDI approach is very effective for numerical analyses of the dynamic J integral in the three-dimensional bodies and provides a refined framework for calculation of dynamic fracture parameters such as dynamic stress intensity factor.

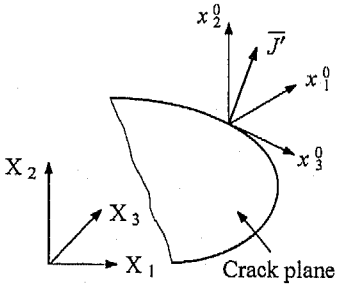


Figure 10: Global and local coordinate systems

5.2 *Dynamic stress intensity factor*

In order to accurately evaluate mixed-mode stress intensity factors, Nishioka and coworkers [Nishioka, Murakami and Takemoto (1990); Nishioha (1994)] developed the component separation method of the dynamic J integral for various crack problems. In the previous paper [Nishioka, Stan and Fujimoto (2002)], the component separation method was extended for three-dimensional cracks to accurately evaluate the three-dimensional stress intensity factor along the dynamically propagating curved crack front.

According to this method the dynamic J integral values can uniquely be converted into the dynamic stress intensity factor as follows:

$$K_M(C) = \delta_M Q_M(C)\overline{K} \quad (M=I, II, III) \tag{23}$$

where M denotes one of the fracture modes. δ_M $(M=I, II, III)$ are the crack opening displacements at a point near the crack tip. C is the crack velocity. The crack velocity functions are defined by

$$Q_I = D(C)/\left\{\beta_1\left(1-\beta_2^2\right)\right\}, \tag{24}$$

$$Q_{II} = D(C)/\left\{\beta_2\left(1-\beta_2^2\right)\right\}, \tag{25}$$

$$Q_{III} = \beta_2; \tag{26}$$

β_1 and β_2 are the crack-velocity parameters normalized by the dilatational wave velocity C_d, and the shear wave velocity C_s, and are defined as $\beta_1^2 = 1 - C^2/C_d^2$ and $\beta_2^2 = 1 - C^2/C_s^2$, respectively. The common part is given by

$$\overline{K} = \left\{\frac{2\mu J'^0_1}{\left(\delta_I^2 Q_I + \delta_{II}^2 Q_{II} + \delta_{III}^2 Q_{III}\right)}\right\}^{1/2} = \left\{\frac{2\mu G}{\left(\delta_I^2 Q_I + \delta_{II}^2 Q_{II} + \delta_{III}^2 Q_{III}\right)}\right\}^{1/2} \tag{27}$$

where μ is the shear modulus.

The features of the component separation method can be summarized as follows:

(i) It can be expressed by the explicit formulas as expressed by Eq. (23).

(ii) It does not require any auxiliary solution field, which is required in the M_1 integral method [Yau and Wang (1984)] that is often used to evaluate mixed-mode stress intensity factors.

(iii) It is applicable using the path independent dynamic J integral, or the dynamic energy release rate.

(iv) The signs of the stress intensity factors are automatically determined by the signs of the corresponding crack opening displacements.

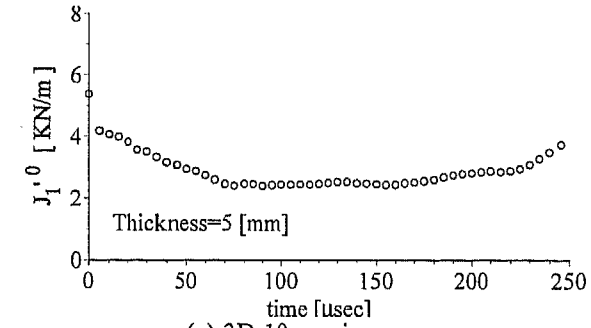
5.3 *Distribution of dynamic J integral*

In the context of fracture mechanics, the path-independence of the dynamic J integral is an important property. For each crack-front segment, the dynamic J integral values were evaluated for three far-field paths (see Fig. 8). The numerical results show excellent path independence for each crack front segment.

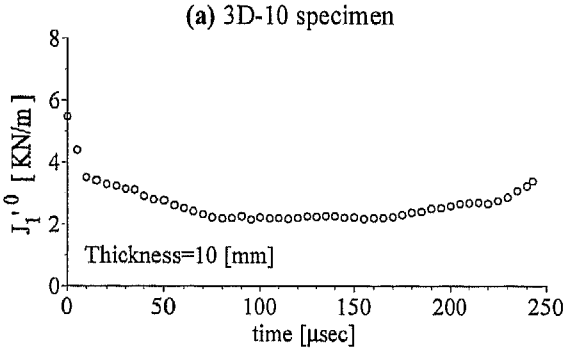
Prior to the dynamic analysis, a static analysis of the specimen is performed according to the experimental sequence [Nishioka, Yoshimura, Nishi and Sakakura (1995)]. Then the crack starts to propagate dynamically from this initial static state of the specimen.

The variations of the dynamic J integral values at the mid-thickness of the plates against the time are summarized in Fig. 11. In all specimens, the dynamic J integral decreases from the static J integral after the fracture initiation, and reaches an almost constant value.

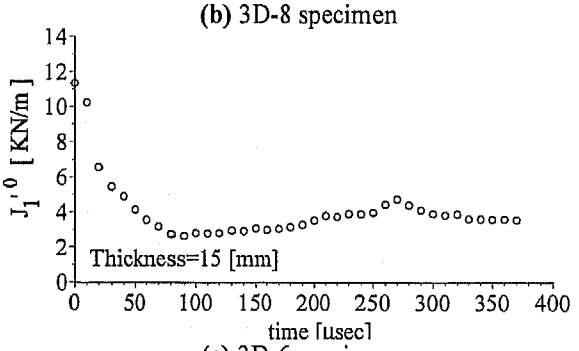
It is pointed out that the tangential component to the crack front, J'^0_3, is almost zero along smoothly curved crack fronts.



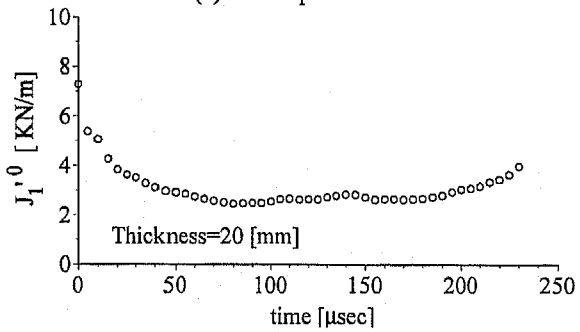
(a) 3D-10 specimen



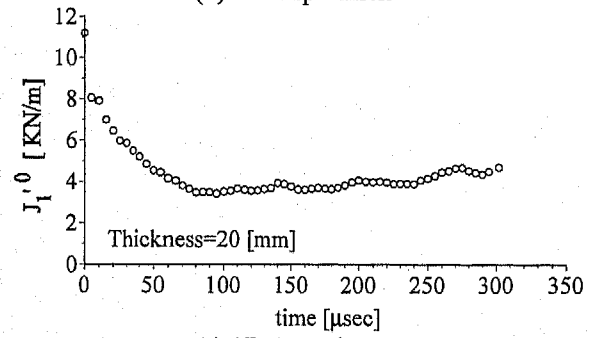
(b) 3D-8 specimen



(c) 3D-6 specimen

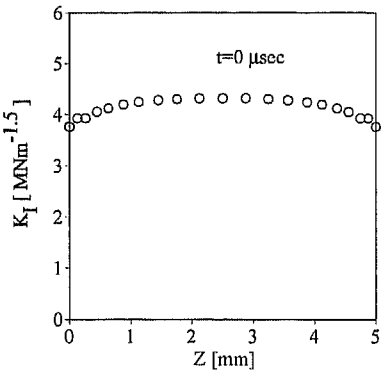


(d) 3D-1 specimen

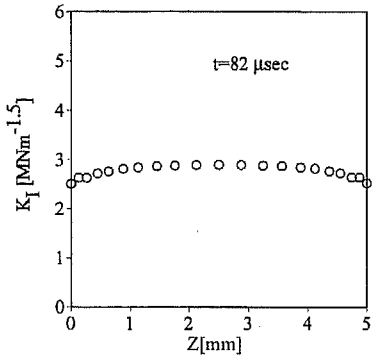


(e) 3D-2 specimen

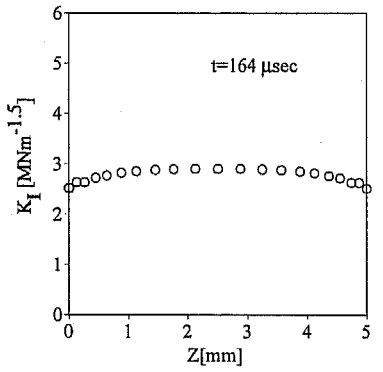
Figure 11: Time variation of dynamic J integral at the mid-thickness of the plate



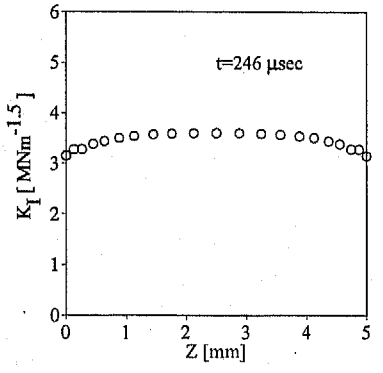
(a)



(b)



(c)



(d)

Figure 12: Distribution of the dynamic stress intensity factor K_I along the propagating crack front (3D-10 specimen)

5.4 *Distribution of dynamic stress intensity factor*

Further insights into the behavior of the crack can be extracted by examining the distribution of the stress intensity factor along the propagating crack front.

The static stress intensity factor as well as the dynamic stress intensity factors during the crack propagation are obtained directly by the component separation method as described earlier (see Eq. (23)). Figures 12, 13, 14, 15 and 16 show the variation of the dynamic stress intensity factor K_I along the crack fronts at various instants of time.

Similar to the responses of the dynamic J integral, in the early stage of dynamic fracture, the dynamic stress intensity factor drops from the apparent static stress intensity factor for the propagated part of the crack front. However, the unbroken crack front keeps almost the same values of the stress intensity factor with the initial static one. The same tendency was observed in all specimens (see Figs. 13(b), 14(b), 15(b) and 16(b)), except 5mm thick specimen, in which the crack front propagates with almost straight crack fronts (see Fig. 3(a)).

In the 5mm thick specimen, for naturally propagating and arresting crack fronts, the stress intensity factors are only slightly higher at the mid-thickness ($Z=0.25mm$) than those at the corner points ($Z=0$ and $5mm$) (see Fig. 5).

In thicker specimens, for these naturally propagating and arresting crack fronts, the dynamic stress intensity factors have almost uniform distribution through the crack fronts. Thus, the mechanism of three-dimensional dynamic fracture can be considered such that the crack front attempts to make a uniform stress intensity factor distribution, even in relatively thick specimens.

The variations of the dynamic stress intensity factors K_I at the mid-thickness of the plates against the time are summarized in Fig. 17. As can be seen from Fig. 17, in each specimen, the dynamic stress intensity factor drops rapidly after dynamic fracture occurred. After certain amount of crack propagation, the natural crack front propagates with a nearly constant K_I value. Furthermore, each crack front arrests with almost constant K_I distribution.

Compared with Figs. 17(d) and 17(e), it may be seen that the level of dynamic stress intensity factor at equivalent time is higher in the 3D-2 specimen than that in the 3D-1 specimen. The higher values of the dynamic stress intensity factor in the 3D-2 specimen are associated with the temperature at which the fracture experiment was performed. As one can see from Table 3, the ambient temperature, T, in the case of the 3D-2 specimen was 22°C, while in the case of the 3D-1 specimen the ambient temperature was 17°C.

Concerning the ambient temperature effect, the results seem to greatly depend upon. An increase of the dynamic stress intensity factor value can be noticed when the ambient temperature increases. The highest dynamic stress intensity factor is obtained in the 3D-6 specimen at the ambient temperature of 28°C.

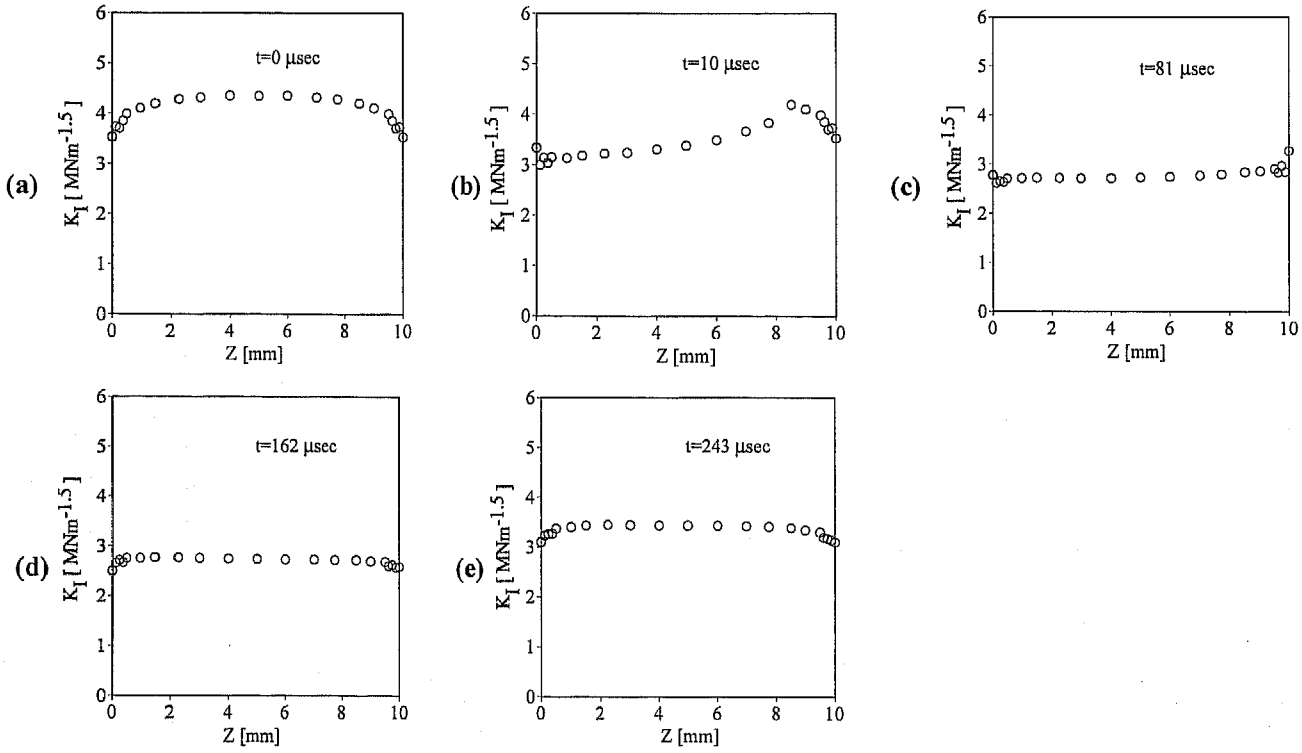


Figure 13: Distribution of the dynamic stress intensity factor K_I along the propagating crack front (3D-8 specimen)

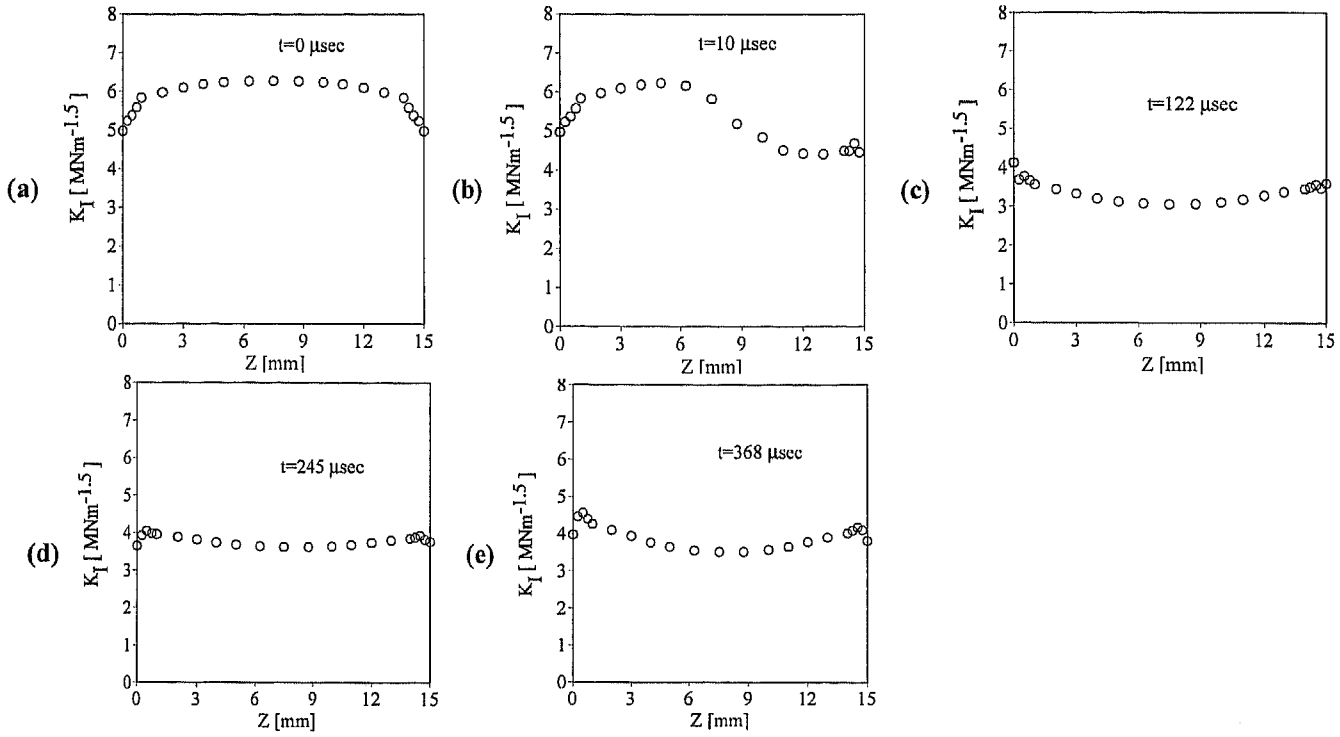


Figure 14: Distribution of the dynamic stress intensity factor K_I along the propagating crack front (3D-6 specimen)

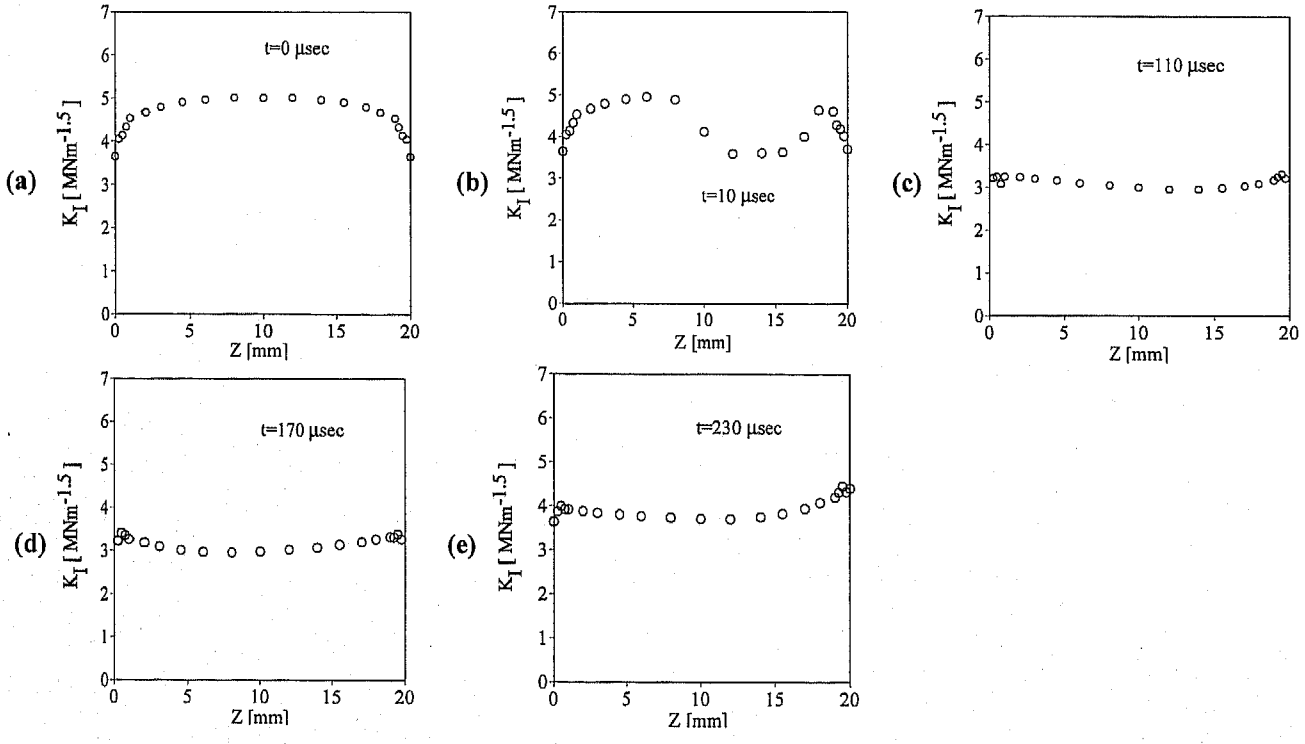


Figure 15: Distribution of the dynamic stress intensity factor K_I along the propagating crack front (3D-1 specimen)

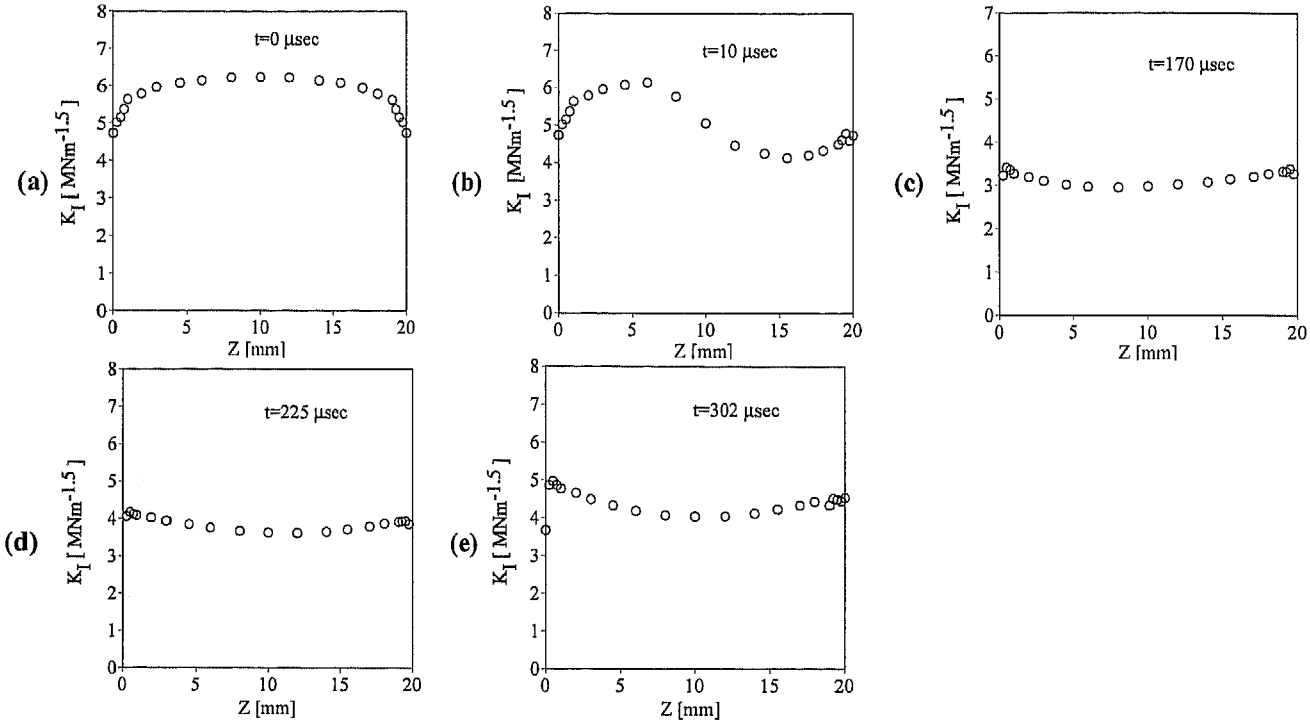
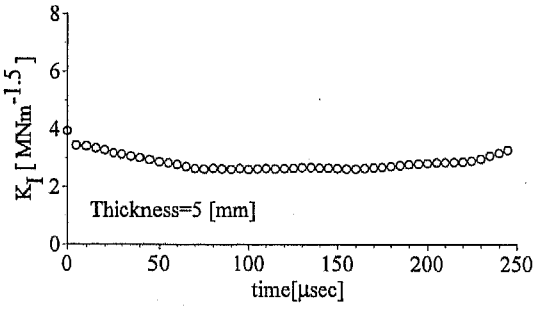
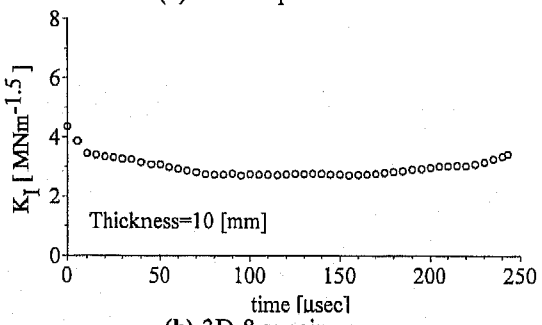


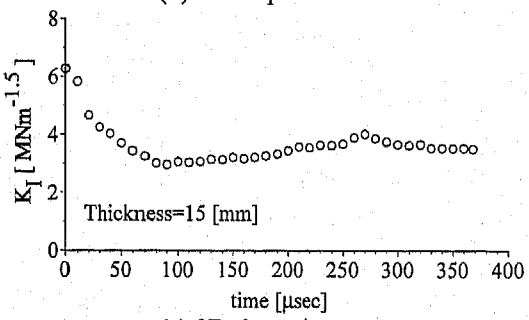
Figure 16: Distribution of the dynamic stress intensity factor K_I along the propagating crack front (3D-2 specimen)



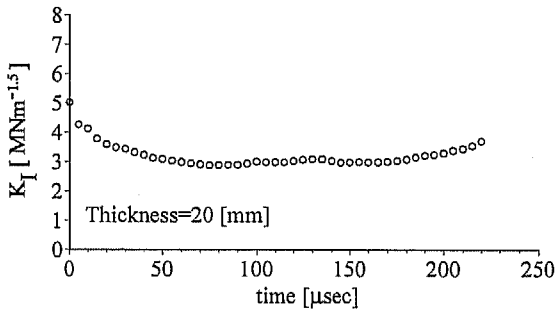
(a) 3D-10 specimen



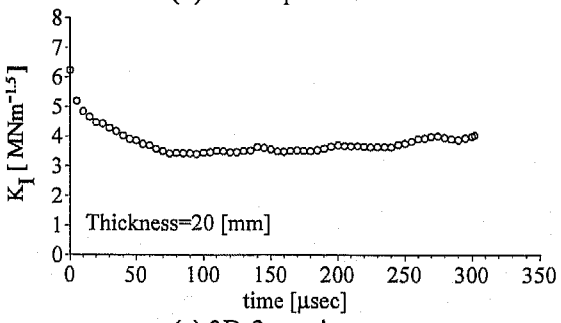
(b) 3D-8 specimen



(c) 3D-6 specimen



(d) 3D-1 specimen



(e) 3D-2 specimen

Figure 17: Time variation of dynamic stress intensity factor (mid-thickness of the plate)

6 Three-Dimensional Stress Fields for Naturally Propagating Cracks

6.1 *Stress variation through thickness*

At the vicinity of the crack tip, there are strong variations of stress fields through the thickness. This indicates the need of a three-dimensional analysis for the study of crack propagation.

The variations of the global stress components σ_{11}, σ_{22} and σ_{33} through the thickness are presented in Figs. 18, 19, 20 and 21. In the figures, the distance along the crack front is normalized by the specimen thickness. The stresses are computed at $r=0.625mm$ ahead of the crack tip in the plane of $X_2 = 0$ (see Fig. 10).

In all specimens, the stress σ_{11} is almost flat except near the free surfaces where the stress drastically drops (see Figs. 18(a), 19(a), 20(a) and 21(a)).

The opening stress σ_{22} near the crack tip has the same trend as the stress σ_{11} (see Figs. 18(b), 19(b), 20(b) and 21(b)). The magnitudes of σ_{22} are almost the same as those of σ_{11}.

Figures 18(c), 19(c), 20(c) and 21(c) show that σ_{33} has a peak value at the center-plane and is close to zero as the free surfaces are approached. In the thicker specimens ($h=15mm$ and $20mm$), for naturally propagating crack fronts, σ_{33} is almost flat except near the free surfaces.

6.2 *Variation of the stress-triaxiality parameter*

The fields near the propagating crack fronts are examined by evaluating the stress-triaxiality parameter defined by

$$\phi = \frac{\sigma_{33}}{\nu(\sigma_{11}+\sigma_{22})}, \tag{28}$$

where ν is the Poisson's ratio. For a state of plane strain, this ratio is equal to unity, whereas it is zero for plane stress. In order to investigate constraint effects in the thickness direction, the global stress components are used in Eq. (28).

The variations of the stress-triaxiality parameter through the thickness are shown in the Figs. 22, 23, 24 and 25. It is seen from the figures that the stress-triaxiality parameter has a peak value at the mid-plane and drastically decays to zero as the free surface is approached. Also, the stress-triaxiality parameter on the mid-plane decays to zero where the distance

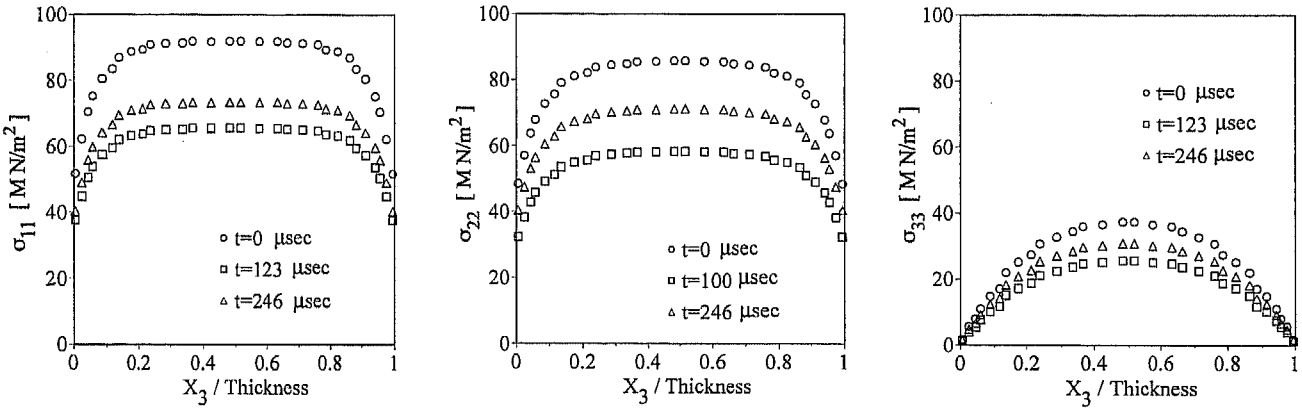


Figure 18: Variation of principal stresses through the thickness ahead of the crack tip (3D-10 specimen: $h=5mm$)

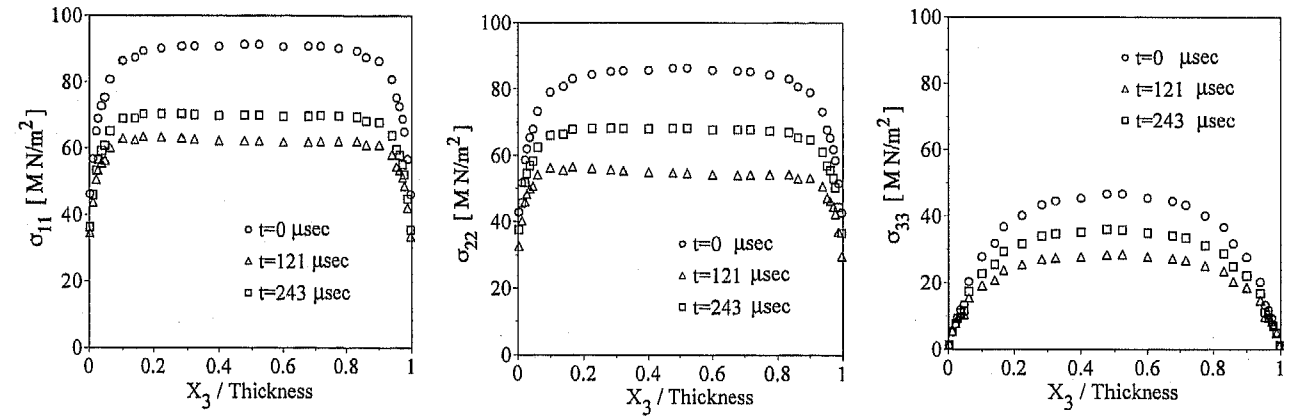


Figure 19: Variation of principal stresses through the thickness ahead of the crack tip (3D-8 specimen: $h=10mm$)

from the crack tip is about one half of the specimen thickness. For static cracks, this feature has been found in literature [Narasihan, Rosakis and Zehnder (1988); Nakamura and Parks (1988)]. To the author's knowledge, in the present study this feature is firstly confirmed for naturally and dynamically propagating curved crack fronts.

In each specimen, the stress-triaxiality parameter for the dynamically propagating crack, has a similar profile with that of the initial state ($t=0\mu sec$), and is slightly lower than the static one. Furthermore, the peak of the stress-triaxiality parameter increases for thicker specimen.

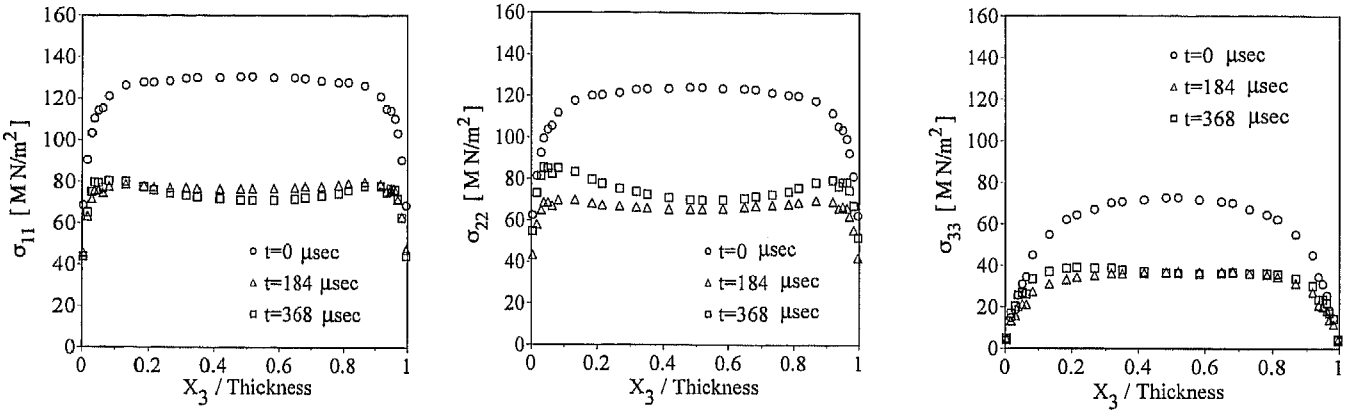


Figure 20: Variation of principal stresses through the thickness ahead of the crack tip (3D-6 specimen: *h=15mm*)

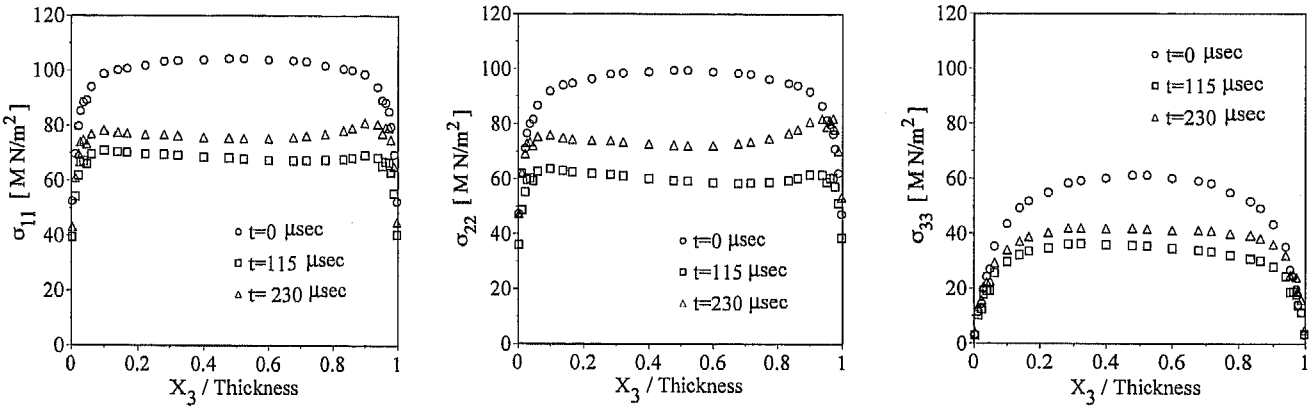


Figure 21: Variation of principal stresses through the thickness ahead of the crack tip (3D-1 specimen: *h=20mm*)

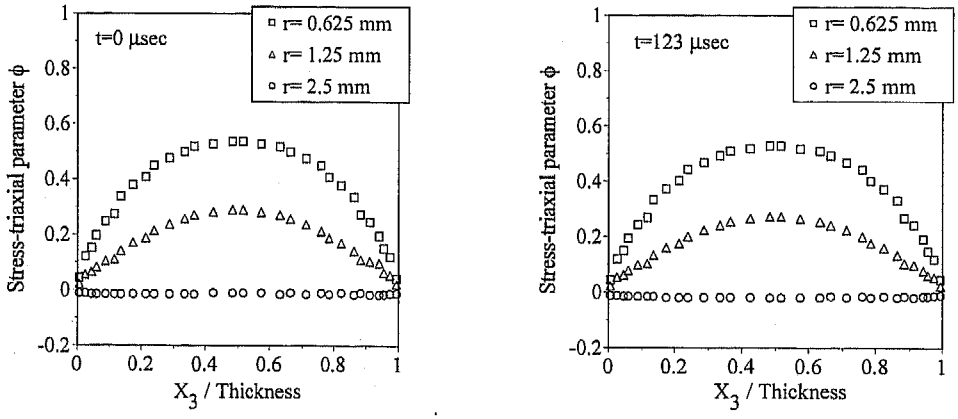
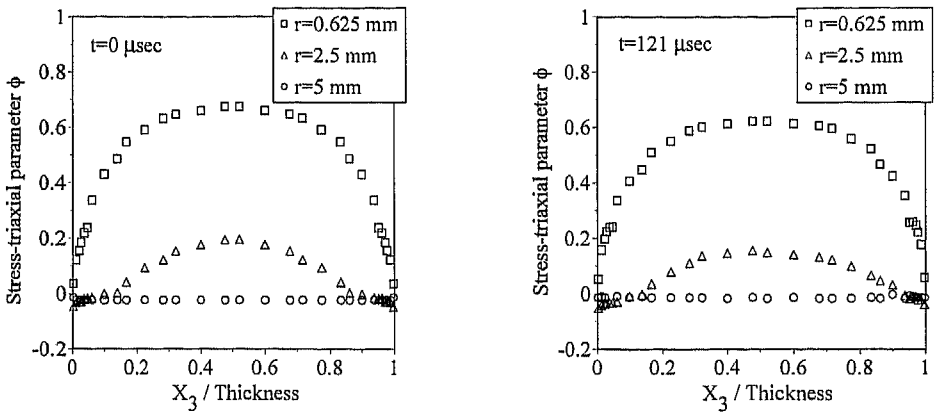
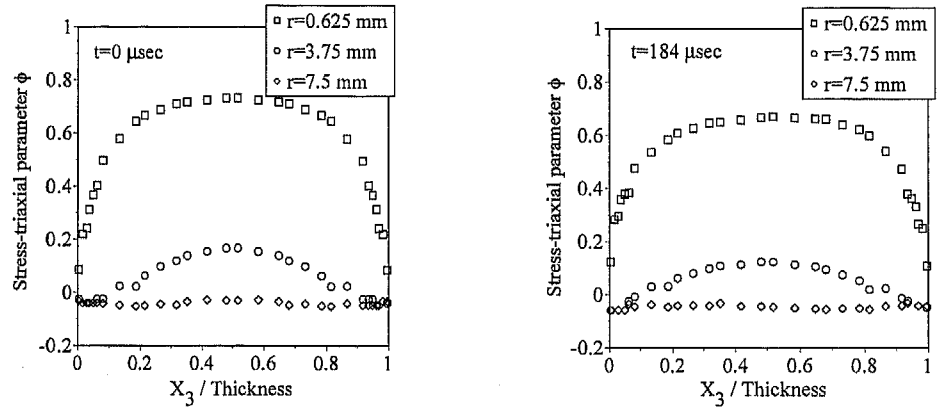


Figure 22: Distribution of the stress-triaxiality parameter through the thickness (3D-10 specimen: *h=5mm*)



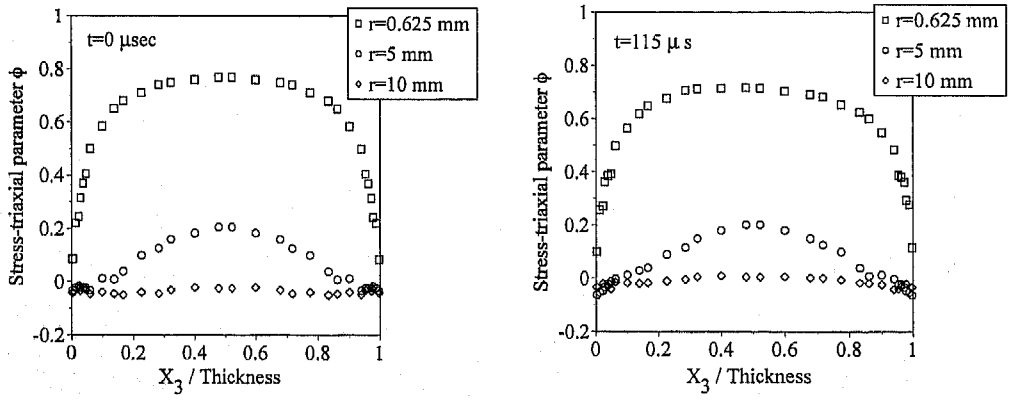
(a) (b)

Figure 23: Distribution of the stress-triaxiality parameter through the thickness (3D-8 specimen: *h=10mm*)



(a) (b)

Figure 24: Distribution of the stress-triaxiality parameter through the thickness (3D-6 specimen: *h=15mm*)



(a) (b)

Figure 25: Distribution of the stress-triaxiality parameter through the thickness (3D-1 specimen: *h=20mm*)

All of these results confirm the characteristics of three-dimensional nature near the crack fronts. It was observed a gradual change from the far-field plane stress condition at nearly the radial distance of a half of specimen thickness from the crack tip, to the plane strain condition at the dynamically propagating curved crack front.

7 Discussion and Conclusions

In this study, based on the experimental conditions and experimentally measured fracture data such as crack propagation history, the generation-phase simulations were

carried out using the moving finite element method, which can exactly model the propagating curved crack front. Then, the dynamic fracture phenomena in the specimens were precisely regenerated in the computational models.

To evaluate the dynamic fracture parameters such as the dynamic J integral and dynamic stress intensity factor along the dynamically propagating curved crack front, the equivalent domain integral method of the dynamic J integral and the component separation method of the dynamic J integral were used.

From the numerically regenerated three-dimensional dynamic fracture events for specimens with different thickness, the distributions of the dynamic J integral and dynamic stress intensity factor along the actual dynamic fracture fronts, in specimens with different thickness, were elucidated.

Due to space limitation, in this paper, only short information about distributions of dynamic J integral was reported. However, the dynamic J integral has similar response to the dynamic stress intensity factor. Details on dynamic J integral distribution will be published elsewhere.

It was found that the dynamic J integral and dynamic stress intensity factor are almost constant along the naturally and dynamically propagating and arresting crack fronts, even at the corner points where the crack front intersects the free surfaces of the plate.

Furthermore, the present results firstly confirm the characteristics of three-dimensional nature up to a distance of approximately half the specimen thickness from the dynamically propagating curved crack front. Irrespective of load level, the stress-triaxiality parameter does not decay to zero until the distance from the crack tip is about one half of the specimen. Also, the triaxiality is lost as the free surface is approached.

Based upon the progress made in this study, the prediction simulations of the formation of crack fronts can be performed. Preliminary results for the crack-front prediction have been already reported by the present authors [Stan, Nishioka and Fujimoto (2002)].

Acknowledgements:

This study was supported by the Grant-in-Aid for Scientific Research (No.14205019) from the Ministry of Education, Science and Culture in Japan, and also by the natural science grant from Mitsubishi Foundation.

References:

Atluri, S.N.; Nishioka, T. (1984), Hybrid methods of analysis. In H. Kardestuncer (ed.) *Unification of Finite Element Methods,* North-Holland, Mathematics Studies 94, pp.65-96.

Atluri, S.N.; Zhu, T. (1998): A new meshless local Petrov-Galerkin (MLPG) approach in computational mechanics. *Computational Mechanics*, vol.22, pp.117-127.

Ching, H.K.; Batra, R.C. (2001): Determination of crack-tip fields by the meshless local Petrov-Galerkin (MLPG) method. *Computer Modeling in Engineering & Sciences*, vol.2, no.2, pp.273-289.

Kanninen, M.F. (1978): A critical appraisal of solution techniques in dynamic fracture mechanics. In D.R.J. Owen and A.R. Luxmoore (ed) *Numerical Methods in Fracture Mechanics*, Pineridge Press, pp.612-634.

Kim, H.G.; Atluri, S.N. (2000): Arbitrary placement of secondary nodes, and error control, in meshless local Petrov-Galerkin (MLPG) method. *Computer Modeling in Engineering & Sciences*, vol.1, no.3, pp.11-32.

Kobayashi, A.S. (1983): Hybrid experimental-numerical stress analysis. *Experimental Mechanics*, vol.23, no.3, pp.338-347.

Nakamura, T.; Parks, D.M. (1988): Three-dimensional stress field near the crack front of a thin elastic plate. *Journal of Applied Mechanics,* vol.55, pp.805-813.

Narasihan, R.; Rosakis, A.J.; Zehnder, A.T. (1988): Three dimensional fields for a through crack in an elastic-plastic solid: numerical analysis and comparison with interferometric measurements. In: A.J. Rosakis, K. Ravi-Chandar and Y. Rajapakse (ed) *Analytical, Numerical. and Experimental Aspects of Three Dimensional Fracture Processes,* ASME Publication, AMD-Vol.91, pp.239-253.

Nikishkov, G.P.; Atluri, S.N. (1987): Calculation of fracture mechanics parameters for an arbitrary three-dimensional crack, by the "equivalent domain integral". *International Journal for Numerical Methods in Engineering*, vol.24, pp.1801-1821.

Nikishkov, G.P.; Park, J.H.; Atluri, S.N. (2001a): SGBEM-FEM alternating method for analysing 3D non-planar cracks and their growth in structural components. *Computer Modeling in Engineering & Sciences*, vol.2, no.3, pp.401-422.

Nishioka, T.; Atluri, S.N. (1980): Numerical modeling of dynamic crack propagation in finite bodies by moving singular elements – part I. formulation. *Journal of Applied Mechanics*, vol. 47, no.3, pp.570-576.

Nishioka, T.; Atluri, S. N. (1982): Analysis of surface flaw in pressure vessels by a new 3-dimensional alternating method. *Journal of Pressure Vessel Technology*, vol.104, no.4, pp.299-307.

Nishioka, T.; Atluri, S.N. (1983a): Path-independent integrals, energy release rates, and general solutions of near-tip fields in mixed-mode dynamic fracture mechanics. *Engineering Fracture Mechanics*, vol.18, pp.1-22.

Nishioka, T.; Atluri, S.N. (1983b): Analytical solution for embedded elliptical cracks, and finite element alternating method for elliptical surface cracks, subjected to arbitrary loadings. *Engineering Fracture Mechanics*, vol.17, no.3, pp.247-268.

Nishioka, T.; Atluri, S.N. (1983c): An alternating method for analysis of surface-flawed aircraft structural components. *AIAA Journal,* vol.21, no.5, pp.749-757.

Nishioka, T. and Atluri, S.N. (1984): On the computation of mixed-mode k-factors for a dynamically propagating crack, using path-independent integrals J'_k. *Engineering Fracture Mechanics*, vol.20, no.2, pp.193-208.

Nishioka, T.; Atluri, S.N. (1986): Computational methods in dynamic fracture. In S.N. Atluri (ed.) *Computational methods in the mechanics of fracture*, Elsevier Science Publishers, Chapter 10, pp.336-383.

Nishioka, T.; Takemoto, Y. (1989): Moving finite element method aided by computerized symbolic manipulation and its application to dynamic fracture simulation. *JSME International Journal*, Series I, vol.32, no.3, pp.403-410.

Nishioka, T.; Murakami, R.; Takemoto, Y. (1990): The use of the dynamic J integral (J') in finite element simulation of mode I and mixed-mode dynamic crack propagation. *International Journal of Pressure Vessels and Piping*, vol.44, pp.329-352.

Nishioha, T. (1994): The state of the art in computational dynamic fracture mechanics. *JSME International Journal*, Series A, vol.37, no.4, pp.313-333.

Nishioka, T. (1995): Recent developments in computational dynamic fracture mechanics. In M.H. Aliabadi (ed) *Dynamic Fracture Mechanics*, Computational Mechanics Publications, Chapter 1, pp.1-60.

Nishioka, T.; Ichikawa Y.; Maeda, N. (1995): Numerical study on three-dimensional dynamic fracture. In: T. Nishioka and J.S. Epstein (ed) *Dynamic Fracture, Failure and Deformation,* ASME Publication PVP-Vol.300, pp.73-85.

Nishioka, T.; Yoshimura, S.; Nishi, M.; Sakakura, K. (1995): Experimental study on three-dimensional dynamic fracture. In: T. Nishioka and J.S. Epstein (ed) *Dynamic Fracture, Failure and Deformation,* ASME Publication PVP-Vol.300, pp.87-97.

Nishioka, T. (1997): Computational dynamic fracture mechanics. *International Journal of Fracture*, vol.86, no.1/2, pp.127-159.

Nishioka, T. (2000): Hybrid numerical methods in static and dynamic fracture mechanics. *Optics Laser Engineering*, vol.32, pp.205-255.

Nishioka, T.; Tokudome, H.; Kinoshita, M. (2001): Dynamic fracture-path prediction in impact fracture phenomena using moving finite element method based on Delaunay automatic mesh generation. *International Journal of Solids and Structures*, vol.38, no.30-31, pp.5273-5301.

Nishioka, T.; Furutuka, J.; Tchouikov, S.; Fujimoto, T. (2002): Generation-phase simulation of dynamic crack bifurcation phenomenon using moving finite element method based on Delaunay automatic triangulation. *Computer Modeling in Engineering & Sciences*, vol.3, no.1, pp.129-145.

Nishioka, T.; Stan, F.; Fujimoto, T. (2002): Dynamic J integral and dynamic stress intensity factor distributions along naturally and dynamically propagating three-dimensional fracture fronts. *JSME International Journal*, Series A, vol.45, no.4 (Special Issue on Fracture Mechanics).

O'Donoghue, P.E.; Nishioka, T.; Atluri, S.N. (1984); Multiple surface cracks in pressure vessels. *Engineering Fracture Mechanics*, vol.20, no.3, pp.545-560.

Stan, F.; Nishioka, T.; Fujimoto, T. (2002): Application-phase simulation of three-dimensional fracture phenomenon. In S.N. Atluri and D.W. Pepper (ed) *Advances in Computational Engineering and Sciences*, Tech Science Press, Chapter 6, Paper 3, pp.1-6.

Yau, J.F.; Wang, S.S. (1984): An analysis of interface cracks between dissimilar isotropic materials using conservation integrals in elasticity. *Engineering Fracture Mechanics*, vol.20, no.3, pp.423-432.

Vijayakumar, K.; Atluri, S.N. (1981): An embedded elliptical flaw in an infinite solid, subject to arbitrary crack-face tractions. *Journal of Applied Mechanics*, vol.48, pp88-96.